Multifunctional Flexible SnTe/MWCNT Crystalline Hybrid for Energy Storage and Humidity Sensing with 3D-Printed Device Integration

Mohammad Saquib [a], Shilpa Shetty [a], Manasa R. Shankar [b], A.N. Prabhu [b], Ramakrishna Nayak [c], M. S. Santosh [d], M. Selvakumar [a]*

[a] Department of Chemistry, Manipal Institute of Technology, Manipal Academy of Higher Education, Manipal 576104, Karnataka, India

[b] Department of Physics, Manipal Institute of Technology, Manipal Academy of Higher Education, Manipal 576104, Karnataka, India

[c] Department of Humanities and Management, Manipal Institute of Technology, Manipal Academy of Higher Education, Manipal, 576104, Karnataka, India

[d] CSIR - Central Institute of Mining and Fuel Research (CIMFR), Digwadih Campus, PO:FRI, Dhanbad-828108, Jharkhand, India.

Correspondence author*: M Selvakumar (selva.kumar@manipal.edu)

Table S1. Composition of SnTe MWCNT polycrystal-based nanocomposites

Material Designation	MWCNT (wt%)	Description
SUM-3	3	SnTe nanoparticles with 3 wt% unwrapped MWCNTs
SUM-5	5	SnTe nanoparticles with 5 wt% unwrapped MWCNTs
SUM-10	10	SnTe nanoparticles with 10 wt% unwrapped MWCNTs
SUM-15	15	SnTe nanoparticles with 15 wt% unwrapped MWCNTs

S1. Screen Mesh Fabrication for Microsupercapacitor and Humidity Sensor Templates

A clean polyester mesh screen is first stretched over a rigid frame and thoroughly degreased and washed to remove any impurities. A uniform layer of photosensitive emulsion is then

applied on the screen using a squeegee, followed by drying in a dark environment to avoid premature curing. A photomask bearing a negative image of the interdigitated design (where the pattern is transparent and the background is black) is prepared and carefully aligned over the emulsion-coated screen. The screen is then exposed to light, which selectively hardens the emulsion in the exposed areas (i.e., the background), while the emulsion beneath the black regions (representing the pattern) remains soluble. Upon rinsing with water, the unexposed emulsion washes away, revealing the open mesh areas in the shape of the interdigitated pattern, allowing ink to pass only through these regions during printing. After drying and applying the shebro screen hardener®, the screen mesh is ready for printing. Conductive ink is then applied to the screen and spread using a squeegee, transferring the interdigitated electrode pattern onto a flexible substrate such as PET. This negative-positive technique offers a reliable and reproducible approach for fabricating miniaturized electrode patterns in flexible electronics, particularly for applications like microsupercapacitors and sensors. The printed devices demonstrated high capacitance, excellent charge-discharge stability, and rapid response times, making the ink suitable for multifunctional applications in energy storage and environmental monitoring [1–6].

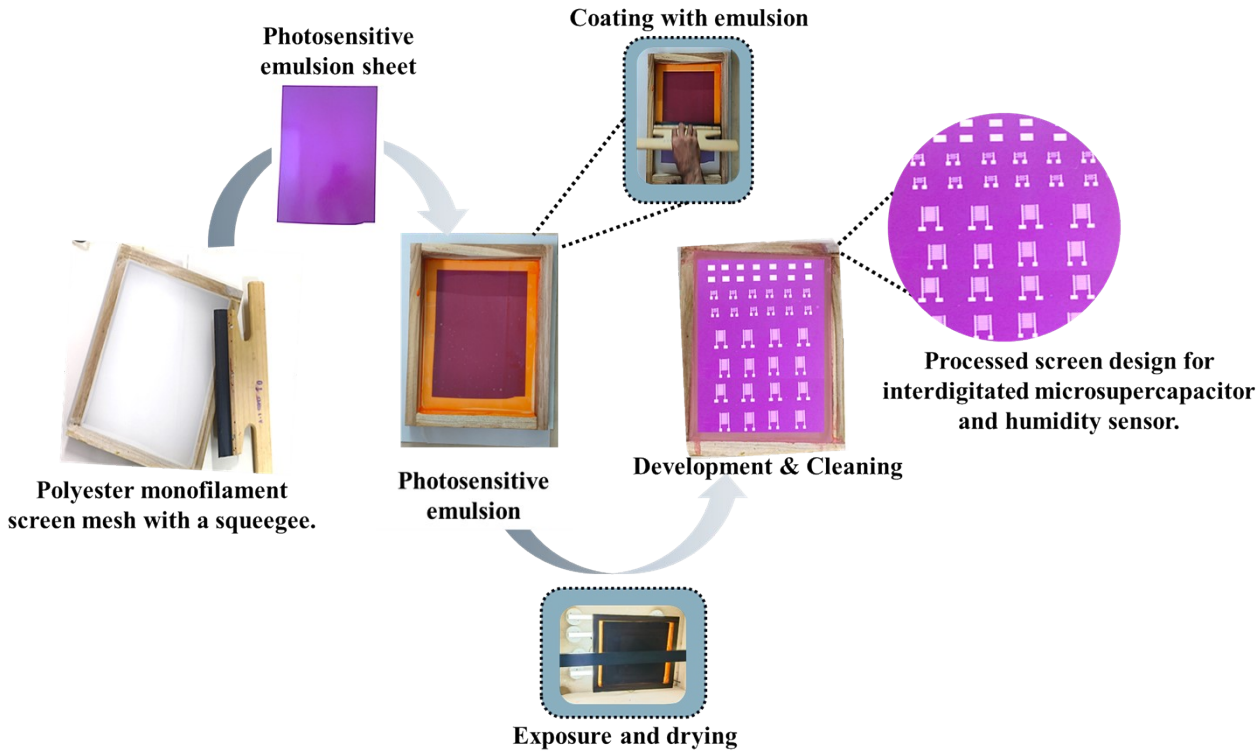

Scheme S1. Schematic of screen preparation via the negative-positive technique for interdigitated electrodes: a mesh is coated with photosensitive emulsion, exposed to UV

through a negative photomask, developed to reveal the stencil, and used for printing conductive inks onto flexible substrates.

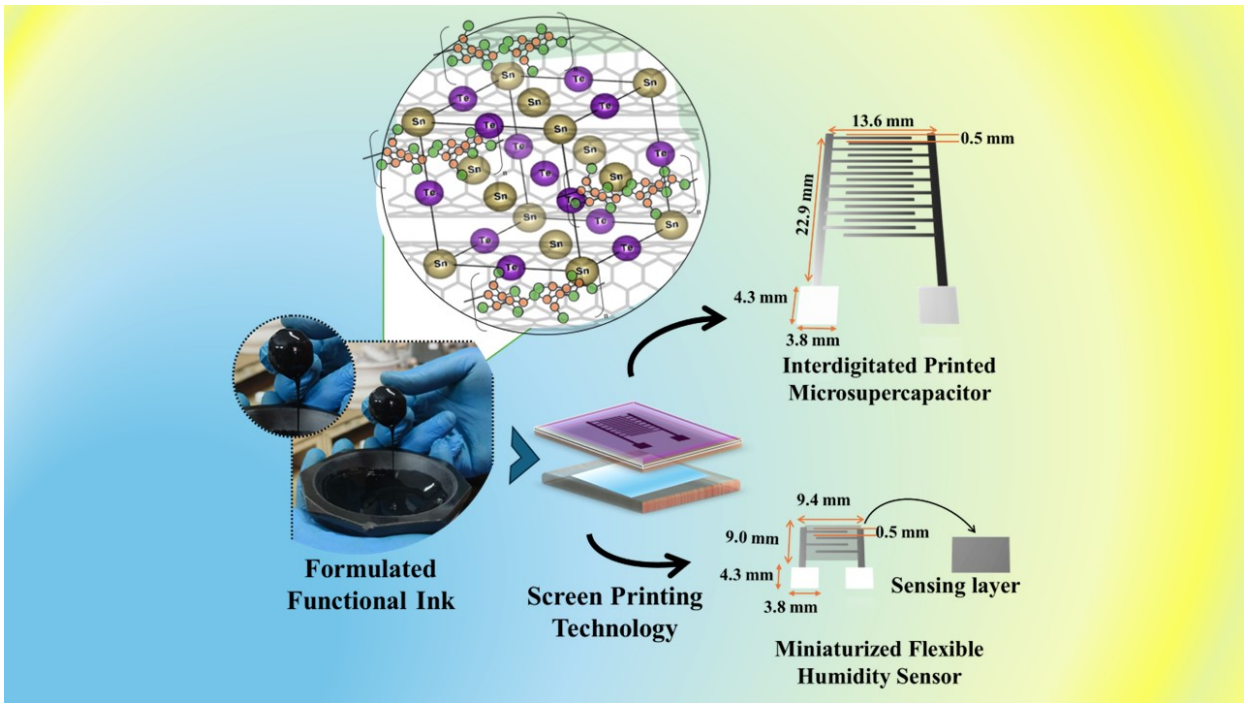

Scheme S2. Schematic of functional conductive ink synthesis and formulation from precursors, followed by screen printing to fabricate interdigitated microsupercapacitors and flexible humidity sensors for energy storage and environmental monitoring.

S2. Characterization Techniques and Performance Evaluation

The phase composition of the synthesized nanomaterials was analyzed using a Miniflex 600 benchtop X-ray diffractometer (Rigaku), utilizing Cu Kα radiation ($\lambda = 0.1542\,nm$) at an operating voltage of $40\,kV$ and current of $15\,mA$. The diffraction patterns were recorded over a 2θ range of $5°$ to $80°$ at a scan rate of $2°\,min^{-1}$ to identify the crystalline structure and phase purity of the materials. Surface morphology and topographical features were examined using Field Emission Scanning Electron Microscopy (FESEM, MAIA3 XMH model) was used to further investigate the surface microstructure and particle distribution. High-resolution transmission electron microscopy (HRTEM) analysis was performed using a JEOL JEM-2100F microscope operating at $200\,kV$ to gain detailed insight into the crystal lattice structure and morphology at the nanoscale. The lattice fringes observed confirmed the high crystallinity of the nanomaterials, while selected area electron diffraction (SAED) patterns verified the polycrystalline nature and phase alignment of the composite materials. X-ray Photoelectron Spectroscopy (XPS) was conducted on a Thermo Scientific $K-Alpha^{+}\,250xi$ system equipped

with a monochromatic $Al\,K\alpha$ X-ray source to determine the elemental composition and chemical states of the surface. The acquired spectra were analyzed using XPS PeakFit 4.1 software, employing a mixed Gaussian–Lorentzian fitting approach. Rheological analysis of the formulated conductive inks was carried out using an MCR 702 MultiDrive Rheometer (Anton Paar, Austria) to evaluate viscosity behavior across a shear rate range of $50 - 700\,s^{-1}$. The inks exhibited shear-thinning behavior, essential for screen-printing applications. The wettability and surface energy of the formulated inks on the PET substrate were determined by static contact angle measurements using an Ossila goniometer, with a measurable angle range of $0 - 120°$. To assess the electrochemical performance of the functional materials (FMs), the electrode materials were initially characterized using a three-electrode configuration via the conventional slurry deposition method. In this setup, the active material-coated electrode served as the working electrode, with a platinum wire as the counter electrode and a saturated calomel electrode (SCE) as the reference. Subsequently, both functional symmetric microsupercapacitor (FSM) and functional asymmetric microsupercapacitor (FAM) devices were fabricated and evaluated using a two-electrode system. In these configurations, the working electrode was composed of the synthesized active nanocomposite, while activated carbon was employed as the counter electrode. Electrochemical analysis was conducted using cyclic voltammetry (CV) and galvanostatic charge–discharge (GCD) techniques to determine specific capacitance, energy and power densities, cycling stability, and Coulombic efficiency Furthermore, the sensing capabilities of the functional materials were evaluated through a series of performance parameters, including sensitivity, response time, recovery time, and stability under varying humidity conditions. These assessments were conducted to explore the multifunctional potential of the developed materials for both energy storage and environmental sensing applications. For humidity sensing studies, a custom-fabricated humidity chamber was utilized. Controlled humidity environments were generated using saturated salt solutions, enabling the creation of specific relative humidity (RH) conditions ranging from 11% to 97% RH. Each RH level was achieved following standard procedures for saturated salt preparation, facilitating accurate evaluation of sensor response under different humidity levels.

Table S2. Shows the various XRD-derived parameters for the enlisted nanocomposites.

Nanocomposites	**Crystallite Size (nm)**	**Dislocation Density** ($\times 10^{-3} nm^{-2}$)	**Microstrain** ($\varepsilon \times 10^{-3}$)

SUM-3	25.82	1.65	3.34
SUM-5	28.17	1.52	3.08
SUM-10	29.06	2.88	4.54
SUM-15	28.04	4.95	5.65

S3. Flexibility and Electrochemical Stability Under Mechanical Bending

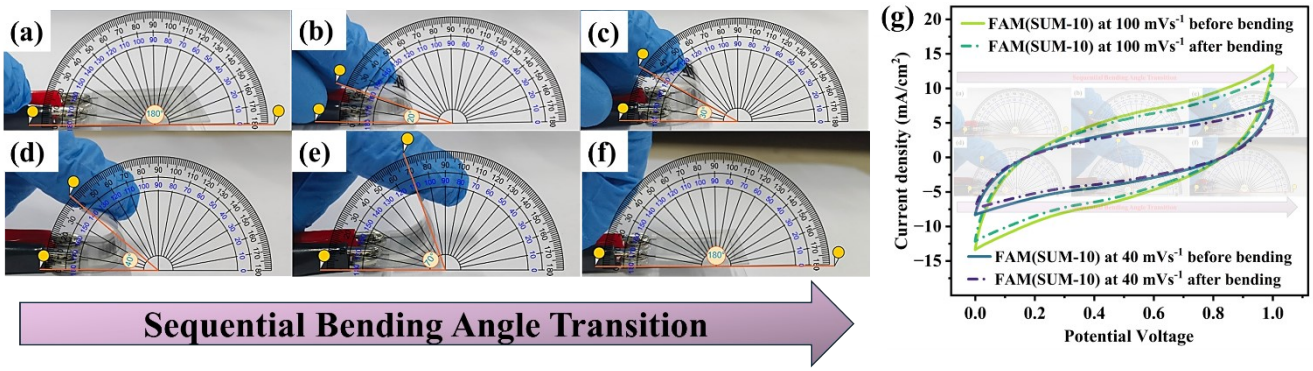

Figure S3(a-f). Sequential bending angle transition of the FAM(SUM-10) device at various angles: **(a)** 180°, **(b)** 70°, **(c)** 30°, **(d)** 40°, **(e)** 70°, and **(f)** return to 180°, demonstrating mechanical flexibility. **(g)** (CV curves of the FAM(SUM-10) device recorded at 40 and 100 mVs^{-1} before and after bending, indicating excellent electrochemical stability under mechanical stress.

S4. Influence of electrode material deposition on device performance

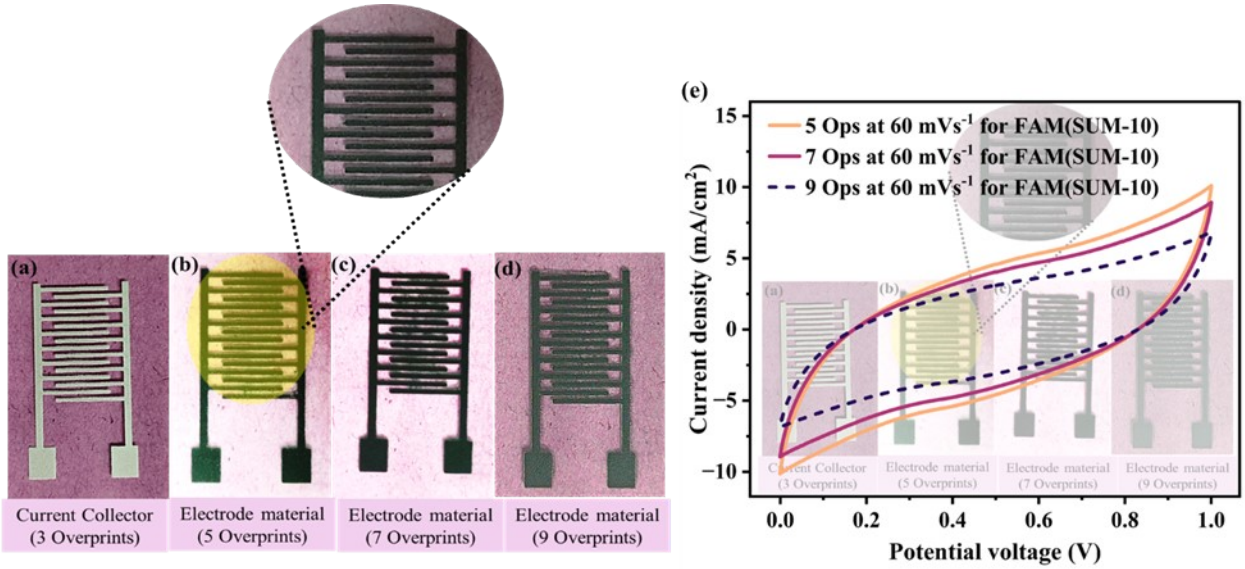

Figure S4(a-e). Photographs of printed microsupercapacitor electrodes with varying overprints (3, 5, 7, and 9 Ops) and their corresponding CV curves at 60 mVs^{-1}.

Table S3. Comparison of the electrochemical properties of different MSCs electrode materials.

Electrode material	**Electrolyte**	**Areal Capacitance ($mFcm^{-2}$)**	**Capacitive Retention (%)**	**Device configuration**	**Ref.**
CuSe@ PANI nanosheet	H_2SO_4/PVA gel electrolyte	308.9 $mFcm^2$	89.80%	Flexible Microsupercapacitors	[7]
CuSe@MnSe	0.5 M Na_2SO_4	164.9 $mFcm^{-2}$	91.62%	Printed flexible supercapacitor	[8]
CuSe@FeOOH// CuSe@MnOOH	PVA-KOH -LiCl gel	20.47 $mFcm^{-2}$	95%	In-Plane Asymmetric MSCs	[9]
(Ni, Co) Se_2 // $Ti_3C_2T_x$	PVA-KOH gel	63 $mFcm^{-2}$	86.4%	Screen-printed flexible MSCs	[10]
(Cu,Co)Se_2	PVA-KOH	58.0 mF cm^{-2}	75%	Screen-printed flexible	
MoS 2 @rGO/CNT	PVA-H_2SO_4	13.7 mF cm^{-2}	96.6%	Spin-coating	[11]
CNT@C//CNT@C	PVA-H_2SO_4	37.1 mF cm^{-2}	68%	wet-spinning method	[12]
VO_x/rGO//G-VNQDs/rGO	LiCl/PVA	207.9 mF cm^{-2}	93.1 %	Direct 3D printing	[13]
$Cu(OH)_2$@FeOOH //$Cu(OH)_2$ @FeOOH	[EMIM][BF_4]$^+SiO_2$	58 mF cm^{-2}	70%	solution-immersion method	[14]
$NiCo_2O_4$//AC	KOH/PVA	35.3 mF cm^{-2}	98.6%	screen-printing process	[15]
Ag@PPy@MnO_2// AC	Na_2SO_4/PVA	95.3 mF cm^{-2}	90.8%	screen-printing technique	[16]

MnHCF-MnO_x/ErGO	LiCl/PVA	16.8 mF cm^{-2}	80.4%	screen printing technology	[17]
Co-Al-LDH//$Ti_3C_2T_x$	KOH/PVA	40 mF cm^{-2}	92%	screen-printing process	[18]
MXene//MXene	PVA-H_2SO_4	61 mF cm^{-2}	-	stamping strategy	[19]
FSM(SUM-10)	1M KOH	91.5 mFcm^{-2}	93.2%	Screen-printed Microsupercapacitor	This work
FAM(SUM-10)	1M KOH	468.6 mFcm^{-2}	96.8%	Screen-printed Microsupercapacitor	This work

Table S4. Controlled RH levels (11 – 97%) were generated using saturated salt solutions in a sealed chamber at 25 °C for sensor testing.

Salt	$LiCl$	$CH3COOK$	$MgCl_2$	K_2CO_3	$Mg(NO_3)_2$	$CuCl_2$	NaCl	KCl	KNO_3	K_2SO_4
%RH	11 %	23%	33%	42%	54%	62%	75%	85%	93%	97%

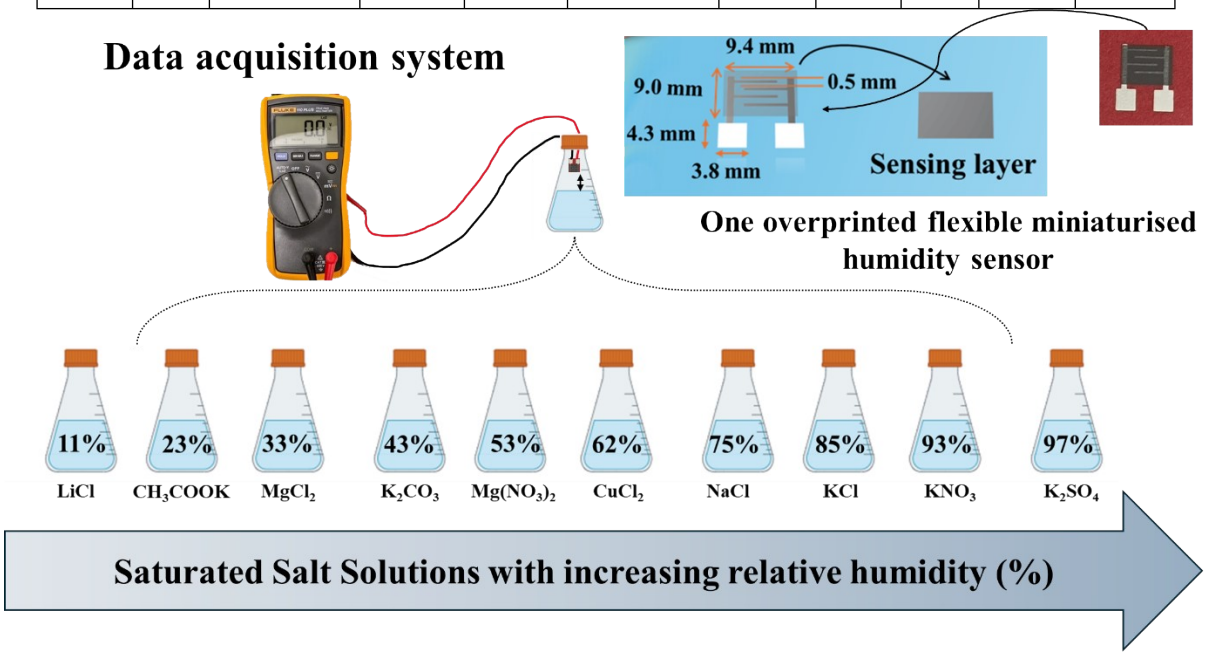

Scheme S4 Experimental setup for evaluating the screen-printed flexible humidity sensor using saturated salt solutions (11–97% RH) and real-time measurements.

S5. The Fabrication of the 3D Printed Assembly for Real-Time Monitoring Applications

The fabrication methodology employed for this real-time monitoring assembly followed established additive manufacturing protocols utilizing computer-aided design (CAD) integration with fused deposition modeling (FDM) technology. The design phase was executed using SolidWorks® 2022 software, enabling parametric solid modeling with precise dimensional control and geometric constraints necessary for the complex assembly. Material selection involved polylactic acid (PLA) thermoplastic polymer filament, chosen for its favourable processing characteristics, including low thermal shrinkage $(0.3 - 0.5\ \%)$, minimal warping tendency, and biocompatibility suitable for electronic device enclosures. The printing parameters were optimized for a Julia Pro Professional FDM printer® manufactured by Fracktal Works®, which provides layer resolution capabilities down to 0.1mm with positional accuracy of $\pm 0.1mm$ in X/Y axes. Pre-processing operations included model slicing and toolpath generation using Fracktory 3D software®, which computed optimal deposition strategies accounting for overhang angles, infill density distribution, and support structure placement to minimize post-processing requirements. The complete assembly dimensions of $130mm \times 100mm \times 75mm$ were successfully fabricated within geometric tolerances of $\pm 0.2mm$, demonstrating the efficacy of integrated CAD-CAM workflows in producing functional prototypes meeting specified design requirements for electronic monitoring applications.

S6. Printing Parameters:

The 3D-printed assembly was fabricated using a $0.4\,mm$ nozzle diameter at an extruder temperature of $210°C$, optimized for polylactic acid (PLA) filament. The layer height was set to $0.4\,mm$, matching 100% of the nozzle diameter to ensure sufficient interlayer adhesion while maintaining reasonable print times. Printing speed was maintained at 50 mm/s to balance surface quality with production efficiency, which is particularly important for complex geometric features. The internal structure employed a 20% infill density with a triangular pattern, providing an optimal strength-to-weight ratio while minimizing material usage and print duration. This infill ensured adequate structural integrity for the monitoring device housing while keeping the assembly lightweight for portable applications. Support structures were designed with minimal contact areas to allow easy removal during post-processing. Collectively, these parameters enabled the successful fabrication of the complete assembly

within specified dimensional tolerances while meeting functional requirements for electronic component integration and mechanical durability.

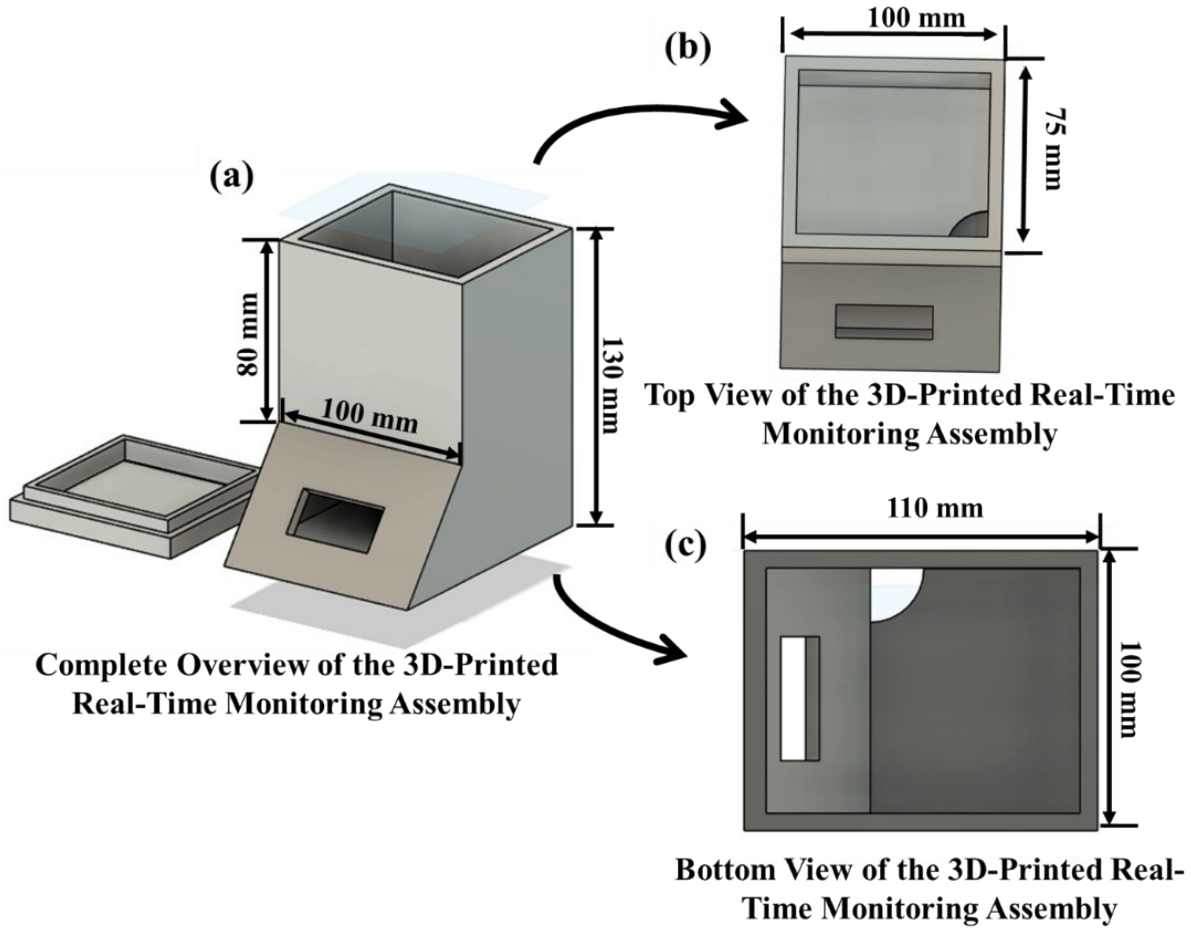

Scheme S5. Complete overview of the 3D-printed real-time monitoring assembly: **(a)** Isometric view showing the cubic device with an open top chamber, enclosure lid, and front-mounted display panel; **(b)** Top view illustrating the internal layout, with the specimen placed in the upper section for analysis; **(c)** Bottom view depicting the base structure, with a rectangular slot housing the microcontroller processor, and the battery positioned to power the system.

Table S5. Shown in the previously reported results for sensing materials for the flexible humidity sensor.

Sensing Material	Interface Structure	RH Range (%RH)	Response Time	Recovery Time	Synthesis Method	Sensing Principle	Ref.
3DAG/PVA/SiO_2	3D Macropores	55-90 %RH	24 s	14.4 s	DC arc plasma jet CVD method	Surface Acoustic	[20]
3D $MoSe_2$@MoS_2 heterojunction	3D Nano Flowers	0-12000 ppm	30 s	33 s	Hydrothermal	Resistive	[21]
3D porous SnO_2-encapsulated MCM48	Cubic Mesoporous	11-98 %RH	9 s	12 s	Hydrothermal	Resistive	[22]
3D porous P4VP	Porous structure	11-95 %RH	2.3 s	22.1 s	Breath figure Method	Impedance	[23]
Thermally reduced graphene oxide powder	Porous structure	6.4 - 97.3 %RH	7 s	13.5 s	Hybrid additive Manufacturing	Resistive	[24]
SnTe/MWCNT (SUM-10)	Nanoparticles over a tubular structure	11- 97 %RH	7 s	9 s	Crystal growth method	Resistive	This work
SnTe/MWCNT (SUM-10) Real-time Sensing	Nanoparticles over a tubular structure	11- 97 %RH	68 s	162 s	Crystal growth method	Resistive	This work

Reference

[1] P. He, J. Cao, H. Ding, C. Liu, J. Neilson, Z. Li, I.A. Kinloch, B. Derby, Screen-Printing of a Highly Conductive Graphene Ink for Flexible Printed Electronics, ACS Appl. Mater. Interfaces. 11 (2019) 32225–32234. https://doi.org/10.1021/acsami.9b04589.

[2] K. Arapov, E. Rubingh, R. Abbel, J. Laven, G. de With, H. Friedrich, Conductive Screen Printing Inks by Gelation of Graphene Dispersions, Adv. Funct. Mater. 26 (2016) 586–593. https://doi.org/10.1002/adfm.201504030.

[3] H. Li, H. Guo, S. Tong, K. Huang, C. Zhang, X. Wang, D. Zhang, X. Chen, J. Yang, High-performance supercapacitor carbon electrode fabricated by large-scale roll-to-roll micro-gravure printing, J. Phys. D. Appl. Phys. 52 (2019) 115501. https://doi.org/10.1088/1361-6463/aafbf3.

[4] R. Nayak, P. Shetty, S. M, A. Rao, K.M. Rao, Formulation of new screen printable PANI and PANI/Graphite based inks: Printing and characterization of flexible thermoelectric generators, Energy. 238 (2022) 121680. https://doi.org/10.1016/j.energy.2021.121680.

[5] D. Li, W. Lai, Y. Zhang, W. Huang, Printable Transparent Conductive Films for Flexible Electronics, Adv. Mater. 30 (2018). https://doi.org/10.1002/adma.201704738.

[6] Y. Yuan, W. Yuan, Y. Wu, X. Wu, X. Zhang, S. Jiang, B. Zhao, Y. Chen, C. Yang, L. Ding, Z. Tang, Y. Xie, Y. Tang, High-Performance All-Printed Flexible Micro-Supercapacitors with Hierarchical Encapsulation, ENERGY Environ. Mater. 7 (2024). https://doi.org/10.1002/eem2.12657.

[7] J.-C. Li, J. Gong, Z. Yang, Y. Tian, X. Zhang, Q. Wang, X. Hong, Design of 2D Self-Supported Hybrid CuSe@PANI Core/Shell Nanosheet Arrays for High-Performance Flexible Microsupercapacitors, J. Phys. Chem. C. 123 (2019) 29133–29143. https://doi.org/10.1021/acs.jpcc.9b08889.

[8] G. Tang, X. Zhang, B. Tian, P. Guo, J. Liang, W. Wu, Hollow heterogeneous CuSe@MnSe for high-performance printed flexible supercapacitor, Chem. Eng. J. 471 (2023) 144590. https://doi.org/10.1016/j.cej.2023.144590.

[9] J.-C. Li, J. Gong, X. Zhang, L. Lu, F. Liu, Z. Dai, Q. Wang, X. Hong, H. Pang, M. Han, Alternate Integration of Vertically Oriented CuSe@FeOOH and CuSe@MnOOH Hybrid Nanosheets Frameworks for Flexible In-Plane Asymmetric Micro-

supercapacitors, ACS Appl. Energy Mater. 3 (2020) 3692–3703. https://doi.org/10.1021/acsaem.0c00150.

[10] B. Balan, M. Narayanasamy, S.P. Rajendra, M.S. AlSalhi, S. Angaiah, Development of Penroseite (Ni,Co)Se 2 and Ti-MXene Inks for Maximizing the Energy Density of Screen-Printed Flexible Microsupercapacitor, Adv. Mater. Technol. 8 (2023). https://doi.org/10.1002/admt.202301329.

[11] W. Yang, L. He, X. Tian, M. Yan, H. Yuan, X. Liao, J. Meng, Z. Hao, L. Mai, Carbon-MEMS-Based Alternating Stacked MoS 2 @rGO-CNT Micro-Supercapacitor with High Capacitance and Energy Density, Small. 13 (2017). https://doi.org/10.1002/smll.201700639.

[12] Q. Meng, H. Wu, Y. Meng, K. Xie, Z. Wei, Z. Guo, High-Performance All-Carbon Yarn Micro-Supercapacitor for an Integrated Energy System, Adv. Mater. 26 (2014) 4100–4106. https://doi.org/10.1002/adma.201400399.

[13] M. Yuan, L. Wang, X. Liu, X. Du, G. Zhang, Y. Chang, Q. Xia, Q. Hu, A. Zhou, 3D printing quasi-solid-state micro-supercapacitors with ultrahigh areal energy density based on high concentration MXene sediment, Chem. Eng. J. 451 (2023) 138686. https://doi.org/10.1016/j.cej.2022.138686.

[14] J.-Q. Xie, Y.-Q. Ji, J.-H. Kang, J.-L. Sheng, D.-S. Mao, X.-Z. Fu, R. Sun, C.-P. Wong, In situ growth of Cu(OH) 2 @FeOOH nanotube arrays on catalytically deposited Cu current collector patterns for high-performance flexible in-plane micro-sized energy storage devices, Energy Environ. Sci. 12 (2019) 194–205. https://doi.org/10.1039/C8EE01979G.

[15] L. Liu, Y. Feng, J. Liang, S. Li, B. Tian, W. Yao, W. Wu, Structure-designed fabrication of all-printed flexible in-plane solid-state supercapacitors for wearable electronics, J. Power Sources. 425 (2019) 195–203. https://doi.org/10.1016/j.jpowsour.2019.03.118.

[16] L. Liu, Q. Tian, W. Yao, M. Li, Y. Li, W. Wu, All-printed ultraflexible and stretchable asymmetric in-plane solid-state supercapacitors (ASCs) for wearable electronics, J. Power Sources. 397 (2018) 59–67. https://doi.org/10.1016/j.jpowsour.2018.07.013.

[17] J. Liang, B. Tian, S. Li, C. Jiang, W. Wu, All-Printed MnHCF-MnO x -Based High-Performance Flexible Supercapacitors, Adv. Energy Mater. 10 (2020).

https://doi.org/10.1002/aenm.202000022.

[18] S. Xu, Y. Dall'Agnese, G. Wei, C. Zhang, Y. Gogotsi, W. Han, Screen-printable microscale hybrid device based on MXene and layered double hydroxide electrodes for powering force sensors, Nano Energy. 50 (2018) 479–488. https://doi.org/10.1016/j.nanoen.2018.05.064.

[19] C. (John) Zhang, M.P. Kremer, A. Seral-Ascaso, S. Park, N. McEvoy, B. Anasori, Y. Gogotsi, V. Nicolosi, Stamping of Flexible, Coplanar Micro-Supercapacitors Using MXene Inks, Adv. Funct. Mater. 28 (2018). https://doi.org/10.1002/adfm.201705506.

[20] Y. Su, C. Li, M. Li, H. Li, S. Xu, L. Qian, B. Yang, Surface acoustic wave humidity sensor based on three-dimensional architecture graphene/PVA/SiO2 and its application for respiration monitoring, Sensors Actuators B Chem. 308 (2020) 127693. https://doi.org/10.1016/j.snb.2020.127693.

[21] W. Guo, Z. He, J. Li, L. Yao, Y. Qiao, F. Wang, Y. Wang, F. Wang, 3D MoSe2@MoS2 heterojunction for humidity sensors to improve sensing performance, J. Alloys Compd. 983 (2024) 173833. https://doi.org/10.1016/j.jallcom.2024.173833.

[22] P. Malik, S. Duhan, R. Malik, A high-performance humidity sensor based on 3D porous SnO 2 -encapsulated MCM-48 for real-time breath monitoring and contactless gesture detection, Mater. Adv. 5 (2024) 2510–2525. https://doi.org/10.1039/D3MA00866E.

[23] J. Dai, H. Zhao, X. Lin, S. Liu, T. Fei, T. Zhang, Humidity Sensors Based on 3D Porous Polyelectrolytes via Breath Figure Method, Adv. Electron. Mater. 6 (2020). https://doi.org/10.1002/aelm.201900846.

[24] F. Ahmed, A. Azhari, E. Marzbanrad, F. Liravi, U. Ali, M.A. Pope, E. Toyserkani, Graphene oxide humidity sensor built entirely by additive manufacturing approaches, J. Mater. Sci. Mater. Electron. 30 (2019) 8980–8988. https://doi.org/10.1007/s10854-019-01226-y.